ORIGINAL RESEARCH ARTICLE

Non-uniform Grain Boundary Migration During Static Recrystallization: A Cellular Automaton Study

FENGXIANG LIN, MATEUSZ SITKO, LUKASZ MADEJ, and LAURENT DELANNAY

During static recrystallization, grains often have non-constant and non-uniform growth rates, significantly affecting the recrystallization kinetics and the microstructure after recrystallization. A cellular automaton model was employed in order to evaluate the relative influences of gradients of stored energy, grain boundary curvature, and heterogeneity of grain boundary mobility on the non-uniform migration of grain boundary segments, leading to the formation of protrusions and retrusions. Electron back-scatter diffraction measurements of a cold-rolled copper microstructure served to feed the model. Orientation maps obtained after partial recrystallization were used to assess the model outcome. The model was capable to predict the shapes of recrystallized grains with retrusions and protrusions. Effects of different model assumptions were compared to reveal individual contributions of different factors to grain size distribution, grain shape and boundary roughness. The model predicted a decreasing average grain growth rate as a result of the progressive immobilization of an increasing fraction of grain boundary segments. The model prediction was compared with experimental results, explaining the origin of stationary boundaries and indicating some further improvements necessary to reach quantitative agreement.

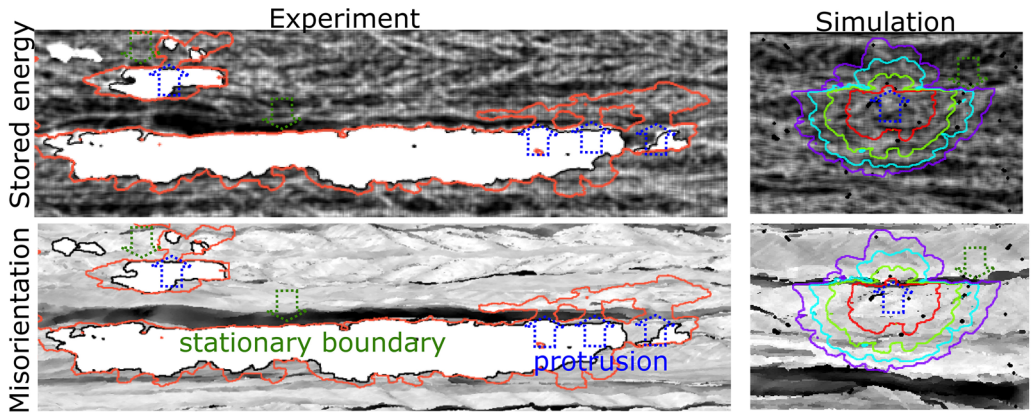

https://doi.org/10.1007/s11661-022-06599-0

I. INTRODUCTION

STATIC recrystallization (SRX) occurs when a deformed material is subsequently annealed. It is a microstructure restoration process during which crystals that are almost defect-free nucleate, and then grow until the deformed matrix is fully invaded. The nucleation behavior and the heterogeneous mobility of grain boundaries may result in different distributions of grain shapes and sizes. As nucleation and growth both critically depend on the thermo-mechanical history of

FENGXIANG LIN is with the Department of Mechanical Engineering, Technical University of Denmark, 2800 Kgs. Lyngby, Denmark and also with the Department of Engineering and Physics, Karlstad Univeristy, 65188 Karlstad, Sweden. Contact e-mail: linfx.cn@gmail.com MATEUSZ SITKO and LUKASZ MADEJ are with the Department of Applied Computer Science and Modelling, AGH University of Science and Technology, Mickiewicza 30 Av. 30-059 Kraków, Poland. LAURENT DELANNAY is with the Institute of Mechanics, Materials and Civil Engineering (iMMC), Université catholique de Louvain, 1348 Louvain la Neuve, Belgium.
Manuscript submitted August 12, 2021; accepted January 9, 2022.

Published online: 13 March 2022

the samples prior to annealing, recrystallization is commonly used to tailor microstructures and improve mechanical properties (*e.g.*, References [1–7]). However, it is still not fullly understood how the kinetics of recrystallization and the characteristics of recrystallized microstructures are affected by different factors.[8–13] Advanced full-field numerical models[14–23] can be used to test various assumptions about the physics determining the microstructural evolution during recrystallization. Such models may contribute to the optimization of annealing processes by allowing sensitivity analyses that are unfeasible experimentally.

Under isothermal annealing, it is usually assumed that growth occurs at constant rates and that nuclei are randomly distributed. Under these assumptions, analytical models indicate that the recrystallized volume fraction (f) increases continuously with time (t) as described by the JMAK (Johnson-Mehl-Avrami-Kolmogorov) equation,[24–26] which was initially proposed to describe phase transformation:

$$f = 1 - \exp\left(-kt^n\right) \qquad [1]$$

When grains grow in three-dimensional space at a constant growth rate, as assumed in the classical JMAK model, the recrystallization kinetics corresponds to Avrami exponents, n, ranging from 3 to 4.[27] However, the Avrami exponents that fit experimental trends are significantly lower in many metals and alloys, *e.g.*, aluminium,[28] copper[12,29] and steel.[11,30] One important reason for such disagreement is that the average growth rate progressively decreases (*e.g.*, Reference [31]), as revealed by computing the Cahn-Hagel growth rate from experimental observations:

$$G_{C-H} = \frac{df}{dt}\frac{1}{S_V} \qquad [2]$$

here S_V is the area per unit volume of recrystallizing grain boundaries (GB), while accounting only GB that have not yet impinged another recrystallized grain.

There are several potential reasons why growth of the recrystallized grains slows down during recrystallization. As a first explanation of the decreasing growth rate during SRX, Vandermeer and Rath[32] suggested that some of the regions with a high dislocation density would recover, and hence the stored energy would be reduced, before being invaded by growing recrystallized grains. However, this mechanism does not apply to some metals and alloys, such as copper, in which simultaneous recovery was found to be negligible [33]. In fact, if the stored energy field is heterogeneous and if regions with high dislocation densities recrystallize first, then the average stored energy decreases with annealing time even in the absence of simultaneous recovery.[34–36] However, Humphreys *et al.* [27] pointed out that growth was influenced by the latter trend only if the stored energy gradients spanned over distances exceeding the average diameter of recrystallized grains. More recently, it was found that the recrystallized grains often grew in a non-uniform manner.[37–39] In a recrystallized grain, different boundary segments migrate with different velocities, leading to the formation of protrusions and retrusions. Lin *et al.*[40] suggested that the average growth rate decreased during recrystallization because of the increasing proportion of boundary segments with low migration velocities, some of which even become stationary. It remains debated whether such immobilized boundary segments are pinned adjacent to regions with low stored energy or whether they rather lack mobility. Both phenomena might actually apply. In addition, according to Zhang *el al.*,[37] since boundary curvature influences the driving force for grain boundary migration, the formation of protrusions and retrusions is likely to change the overall growth rate.[41]

The Monte Carlo,[14] cellular automaton,[15] level-set,[16,17] vertex,[18] and phase-field[22,23] models are examples of numerical approaches that can be adopted to evaluate the relative contributions of stored energy and boundary mobility to the recrystallization kinetics. Such models aim to predict the shapes and sizes of recrystallized grains as well as the resulting texture. The cellular automaton (CA) technique, which was selected for the present study, builds upon several contributions including the model of Hesselbarth[42], precursor of the application of CA to investigate SRX, followed by Davies[43] and Goetz,[44] and then Raabe,[45] who introduced probabilistic transition rules in a three-dimensional CA model. Models have been further developed and applied to study SRX in different metals, including aluminium,[46] copper alloys,[47] and steel.[48] This has progressively contributed to a better insight into the underlying physical processes. Kazeminezhad *et al.*[49] investigated the influence of grain geometry on recrystallization kinetics. Han *et al.*[50] considered not only grain shapes but also the influence of substructure within particular grains. Mukhopadhyay[51] addressed three types of preferential sites for nucleation: grain boundaries, transition bands, and embedded particles. Instead of assuming either a homogenous or an artificially/stochastically distributed heterogeneous microscopic fields of stored energy and lattice orientations, crystal plasticity-based finite element modelling (CPFEM) was used to feed SRX simulations relying on a CA model[52] and a phase-field model.[22] Comprehensive reviews of the CA approach applied to grain growth can be found in References [53] and [54]. Also, from the algorithmic point of view, a significant progress was recently made in order to reduce the computational time of such models.[55]

The numerical study presented here aims to reproduce the heterogeneity of grain boundary migration during the recrystallization of cold-rolled copper samples, and to investigate effects of various microstructural factors on grain growth. In a preliminary experimental investigation,[40] microstructural evolution during recrystallization was probed *ex-situ* using electron back-scatter diffraction (EBSD). It was found that the initial growth rate was large, but it then progressively dropped down to very low values due to accumulation of stationary boundary segments. *Ex-situ* EBSD analysis indicated that stationary and mobile boundary segments tend to have different stored energy distribution in front of them and also different misorientations to the deformed matrix. However, experimentally, it was not possible

to evaluate separately the contributions of different factors to the growth of recrystallized grains. This analysis is thus resumed in the present study based on full-field numerical simulations.

The originality of the present study is to feed the CA model with the distribution of stored energy and the lattice orientation map obtained directly from EBSD measurements. Different variants of the model are used in order to identify and understand the effects of stored energy, boundary mobility, and boundary curvature. The implications of performing such numerical predictions in 2D, whereas the real microstructure is 3D, are discussed too.

II. EXPERIMENTS

A. *Material*

The material used in this work is oxygen-free high conductivity copper (99.95 pct purity) with an initial grain size of 22 μm. More details of the initial material can be found in Reference [56]. A sample which was 5 mm thick, 44 mm wide and 100 mm long, was cold-rolled to a thickness reduction of 90 pct in multiple passes. For each pass, the ratio of the contact length over the average plate thickness was kept between 0.5 and 5 to ensure a rather homogeneous deformation across the roll gap.[57,58]

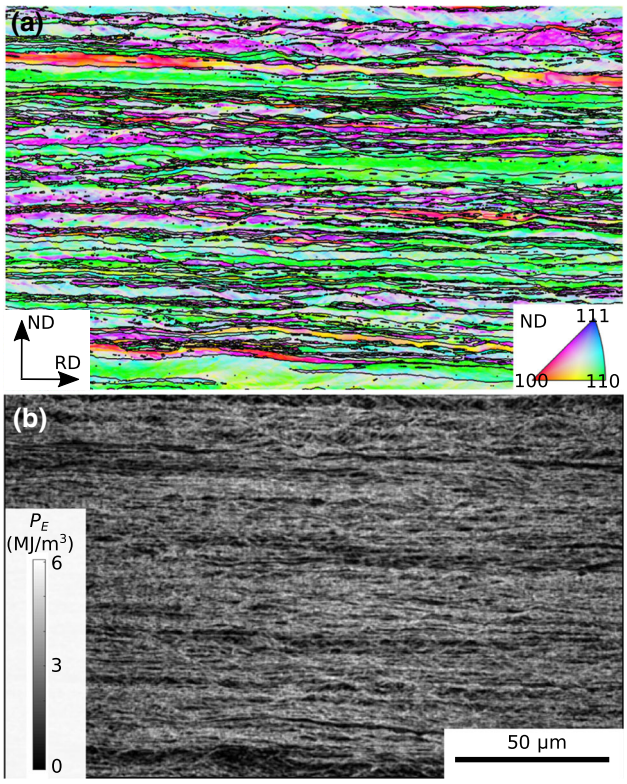

Fig. 1—Microstructure of a copper sample cold-rolled to 90 pct thickness reduction. (*a*) Orientation map with colors corresponding to the inverse pole figure (IPF) of the normal direction (ND). The black lines represent boundaries with a misorientation higher than 15°. (*b*) Map showing the microscopic heterogeneity of the stored energy (P_E).

B. *Characterization of Deformed Microstructure*

A small piece was cut from the center of the rolled plate. The longitudinal section was ground and electro-polished. Microstructure after deformation was characterized using EBSD with a step size of 0.1 μm covering an area of 160×99.6 μm^2. As shown in Figure 1(a), the microstructure after deformation consists of bands parallel to the rolling direction (RD). The average band thickness is 0.6 μm when measured as the average intercept length along the normal direction (ND) considering boundaries with misorientations higher than 15° .

Godfrey *et al.*[59] suggested a method to estimate the stored energy (P_E) from the misorientations revealed by EBSD, assuming that, plastically deformed samples store energy mostly in dislocation boundaries and high angle boundaries. For this, it was assumed that the misorientations measured between adjacent pixels of the orientation map corresponded to dislocation boundaries with an energy (γ) deduced from the Read-Shockley equation[60]:

$$P_E = \frac{s}{r^2}\sum_i \gamma(i) \quad \text{where}$$
$$\gamma(i) = \begin{cases} \gamma_c \dfrac{\theta(i)}{\theta_m}\left(1 - \ln\left(\dfrac{\theta(i)}{\theta_m}\right)\right) & \theta < \theta_m \\ \gamma_c & \theta \geq \theta_m \end{cases} \quad [3]$$

The s parameter designates the step size of the EBSD map whereas the $\gamma(i)$ values were obtained by considering every pair of adjacent pixels with a misorientation $\theta(i)$ higher than 2 deg inside a square-shaped kernal of size $r = 0.7$ μm centered on the location of interest. Such misorientations were calculated as the minimum rotation angle bringing one crystal lattice onto the other, while accounting for the crystal cubic symmetry. In pure copper, high angle boundaries (HABs) with a minimum misorientation $\theta_m = 15°$ have an energy per unit area equal to $\gamma_c = 0.625$ J/m^2. This method to estimate stored energy is suitable for metals that form cell/lamellar structures after plastic deformation, such as alumnium, copper and nickel.[61,62] As such, the stored energy P_E can also be associated with a geometrical necessary dislocation (GND) density through the Read-Shockley relationship.[63] As shown in Figure 1(b), the here computed stored energy field tends to reproduce the grains' banded topology, *i.e.*, some bands host higher stored energy than others. It is noted that this method tend to underestimate the stored energy because it considers only contributions from dislocation boundaries with misorientation angles larger than 2 deg, but the stored energy map obtained by this method reflects the stored energy variation in the material.

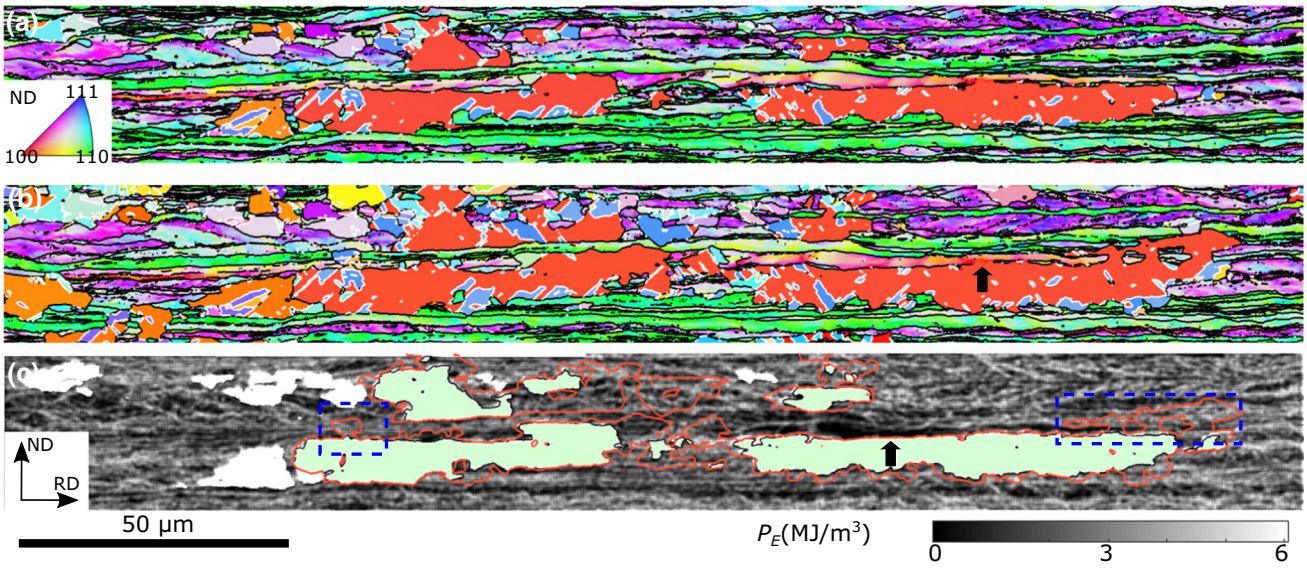

Fig. 2—Close up on the partially recrystallized microstructure after *ex-situ* annealing at 423 K. (*a*) IPF map after 10 minutes annealing. (*b*) IPF map after 10 + 25 minutes annealing. (*c*) Local distribution of the stored energy determined using the EBSD data after the first annealing step. All the parts belonging to the largest recrystallized grain after the first annealing step are colored light green, while boundaries of the same grain after the second annealing step are plotted on top of stored energy map and shown by red lines. The white parts in (c) belong to other recrystallized grains after first annealing step. The black lines in (a) and (b) represent boundaries with a misorientation higher than 15 deg, whereas the white lines represent twin boundaries. The arrow in (b) marks a place where the boundary segments stop near a deformed band with a low misorientation to the recrystallized grain. The arrow in (c) marks a place where the boundary segments stop near a low stored energy region. The dotted rectangles show two places with protrusions that bridge across a unfavorable band and allow reaching another deformed band (Color figure online).

C. *Ex-situ EBSD Characterization*

The polished cold-rolled sample was enclosed in a vacuum glass tube with 50 kPa Ar (purity 99.999 pct), and annealed in an air furnace at 423 K for 10 minutes. Several regions where recrystallized grains appeared were characterized using EBSD with a step size of 0.1 μm. The sample was then placed in a vacuum glass tube again and annealed at 423 K for 25 minutes, after which the same regions were scanned again using EBSD with the same step size. EBSD maps after the first and the second annealing steps were compared to study growth of individual grains. To achieve this accurately, the first EBSD map were corrected with respect to the second EBSD map *via* affine transformation using the method proposed in Reference [64].

Recrystallized grains were identified manually according to the following steps: Firstly, grains were reconstructed from the EBSD data using a threshold misorientation of 2 deg. Secondly, grains separated by twin boundaries were merged, while defining twin boundaries as boundaries with a maximum deviation of 1 deg from $60° < 111 >$. Thirdly, recrystallized grains were identified manually. Lastly, crystal orientations were analyzed, and if two recrystallized regions had the same orientation (maximum difference of 0.5 deg), they were merged into one grain. The last step was necessary because, due to the irregular 3D shapes, some recrystallized grains are likely to appear disconnected in the 2D cross-section of the map.

Figure 2 shows a typical region containing several recrystallized grains. One recrystallized grain is much larger than the others: it measures 150 μm along the rolling direction (RD) and about 30 μm along the normal direction (ND). This grain is colored light green in Figure 2(c), while boundaries of the same grain after the second annealing step are shown by red lines in Figure 2(c). The lattice orientation of this large grain is close to the Cube orientation (red in Figures 2(a) and (b)) and it hosts many small annealing twins (blue in Figures 2(a) and (b)), which have developed during the growth. This grain has a very irregular shape, which results from the non-uniform migration velocity of different boundary segments. In Figure 2, the grain appears subdivided into several islands, but these sub-regions would certainly connect if the map was shifted along the third dimension. When comparing to the previous orientation maps, it is found in Figure 2(c) that 47 pct of the boundary segments surrounding the large grain are stationary even though they are in contact with a deformed matrix, *i.e.*, they are immobilized before impinging another recrystallized grain. Stationary boundary segments are defined as those with a displacement less than 2 pixels (0.2 μm) during the second annealing step. The motion of some of the stationary boundary segments, marked by an arrow in Figure 2(c), may be hindered by a low stored energy region. Other stationary segments, marked by an arrow in Figure 2(b), may have low mobility because the local lattice orientations inside the deformation band are close to the Cube orientation, *i.e.*, the orientation pinning effect.[65,66] Another noteworthy feature is that some protrusions form on the stationary boundary segments, as marked by the dotted rectangles in Figure 2(c). These protrusions bridge a locally

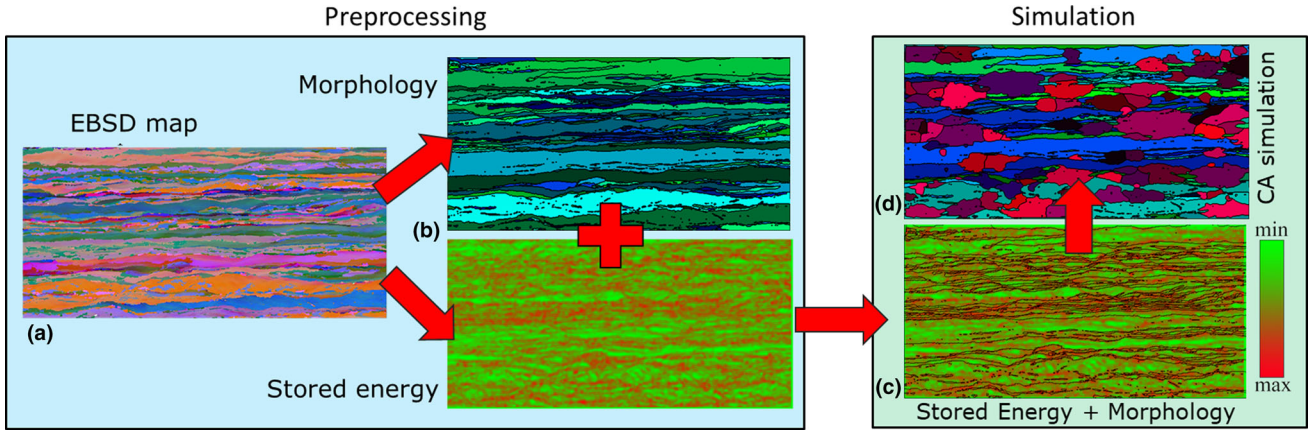

Fig. 3—EBSD data for subsequent immersion procedure: (*a*) Euler angles, (*b*) accumulated strain and grains morphology and (*c*) input data for the CA simulation, (*d*) examples of the simulation results.

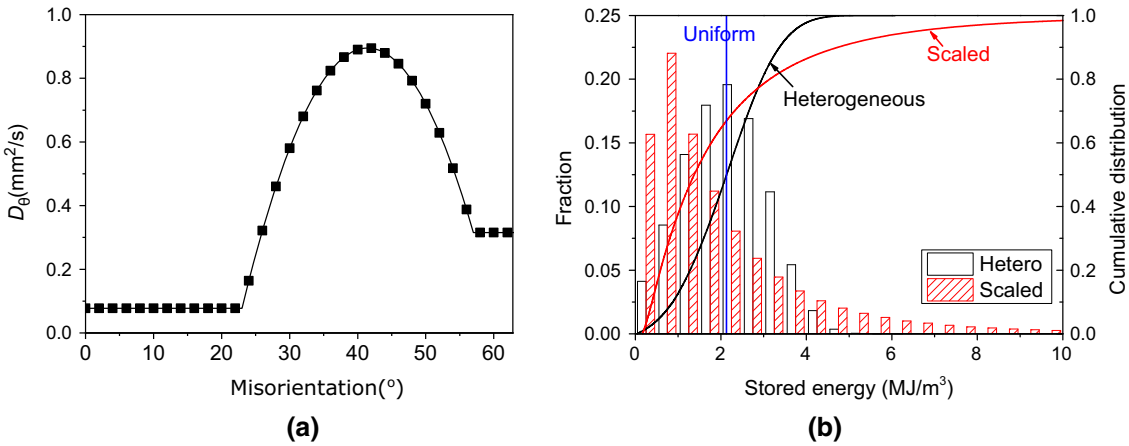

Fig. 4—(*a*) Dependence of the reference diffusion coefficient D_θ on the misorientation angle θ. The reference diffusion coefficient for $\theta \leq 23°$ and $\theta \geq 57°$ is assumed to be constant. (*b*) Three distributions of local stored energy used as input of the CA model: the heterogeneous stored energy field measured experimentally (the same as Fig. 1(b)), a uniform field, and a scaled field amplifying the microscopic heterogeneity.

unfavorable region until the recrystallized grain reaches another region where growth is eased. Some other examples were reported in previous works.[40,56] It should be noted that the overall recrystallized area fractions after the first and second annealing steps are 5 and 10 pct, respectively. In Figure 2, the largest grain alone counts for a large portion of the map area.

III. MODEL DESCRIPTION

The orientation map shown in Figure 1(a) served as input for the CA simulation. The banded cold-rolled microstructure was thus fully immersed into the numerical model. Each pixel of the EBSD scan was represented by one CA cell with the same experimentally measured local lattice orientation. The cell size is thus 0.1 μm, and altogether the cells formed a square grid in the automaton of 1600×996 cells. The concept of the image-based SRX calculations is shown in Figure 3.

The selected CA model is described in detail in Reference [54], and only the major assumptions are recalled below. As is commonly done,[27] the velocity of each segment at the boundary of a recrystallized grain was computed as the product of a mobility M_G and a - so-called - net pressure scaling with the driving force for grain growth: $v_i = M_G P$. The value of M_G depended on the misorientation θ between the two adjacent cells in the CA grid and on the temperature T. It was computed as:

$$M_G = \frac{D_\theta b^2}{k_B T} \exp\left(-\frac{Q_G}{k_B T}\right), \qquad [4]$$

where k_B is the Boltzmann constant, $b = 2.56 \times 10^{-10}$m is the Burgers vector, $Q_G = 1.428 \times 10^{-19}$J is the activation energy for grain boundary motion, and D_θ is a reference diffusion coefficient. The reference diffusion coefficient was assumed to depend on the misorientation angle of the grain boundary, as represented in Figure 4(a). This dependence was proposed based on the experimental measurement of grain boundary mobilities for boundaries with the <111> rotation axis.[67] Outside the range of experimental data, D_θ was

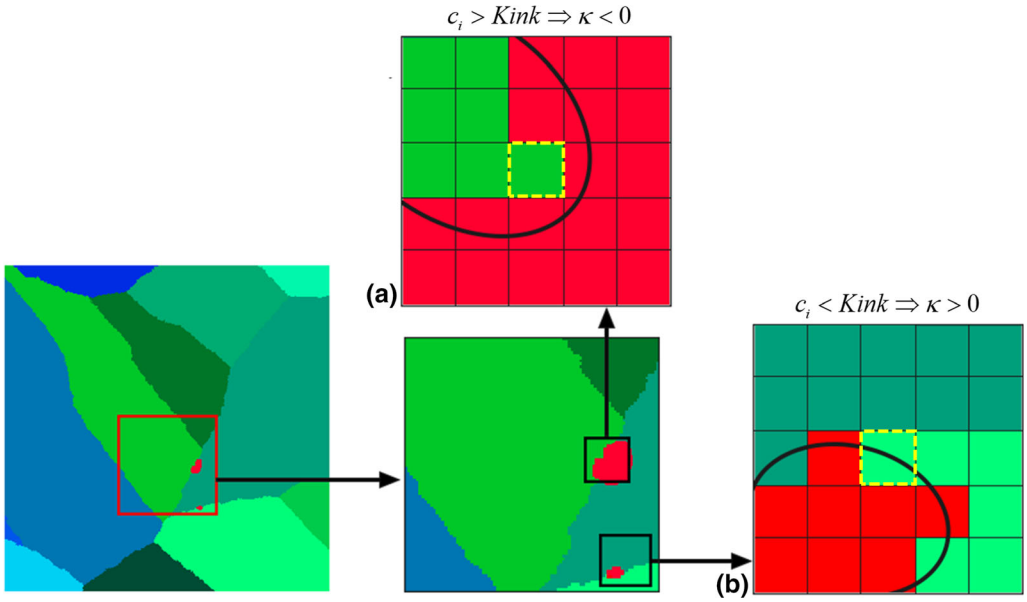

Fig. 5—Examples showing calculation of grain boundary curvatures. (*a*) an example with a negative boundary curvature. (*b*) an example with a positive boundary curvature.

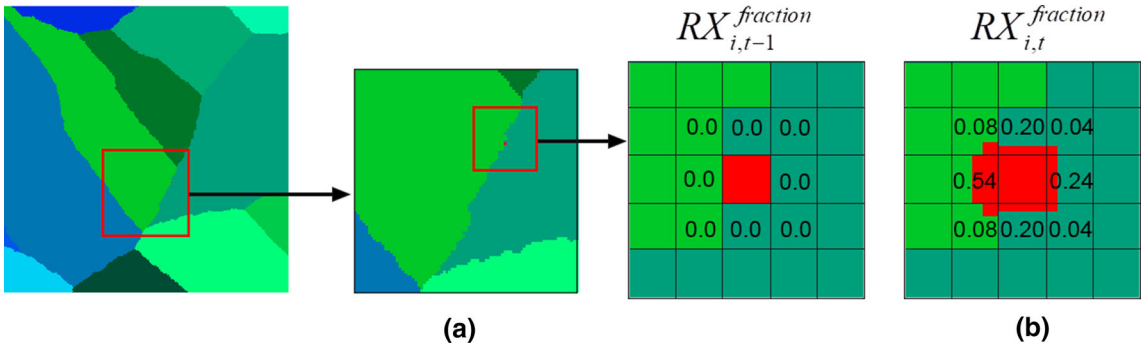

Fig. 6—Evolution of recrystallization volume fraction after a single CA time step. (*a*) Recrystallization at the time step $t-1$. (*b*) Recrystallization at the time step t.

assumed to be constant. All this was meant to capture the heterogeneous mobility for high angle boundaries, even though the misorientation axis was ignored in the present work.

The model accounted for two major driving forces for SRX:

$$P = \Delta P_E + P_{GB} = \Delta P_E - \gamma_{GB}\kappa \qquad [5]$$

The first term, ΔP_E, is the difference of stored energy across the grain boundary, whereas P_{GB} is a capillarity force, proportional to both the GB interfacial energy γ_{GB} (already introduced in Eq. [3]) and the GB curvature κ. When the GB of the recrystallized grains bulged outward, the value of κ was positive, and thus refraining grain growth. In the present model, effects of solute drag were not considered because the material considered is high purity copper, for which solute drag is usually not considered to have a significant effect.[68]

The calculation of grain boundary curvature is schematically presented in Figure 5. The same procedure was applied for both boundaries between recrystallized–recrystallized and recrystallized–unrecrystallized pairs of grains. This calculation method is well adapted to CA on a square grid, as described in Reference [69]:

$$\kappa = \frac{A}{C_S}\frac{Kink - c_i}{N'} \qquad [6]$$

Here C_S is the CA cell size, $A = 1.28$ is a topological parameter[70], $N' = 5 \times 5 - 1 = 24$ is the number of neighboring cells, out of which c_i are recrystallized, whereas $Kink = 3 \times 5 = 15$ is the number of recrystallized cells expected in case of a flat interface.

Grain growth was predicted by relying on a transition rule that determined which ones of the CA cells (*i.e.*, pixels) adjacent to the recrystallized grains were invaded first. Within each CA cell belonging to the deformed matrix, the recrystallized area fraction f_i evolved progressively:

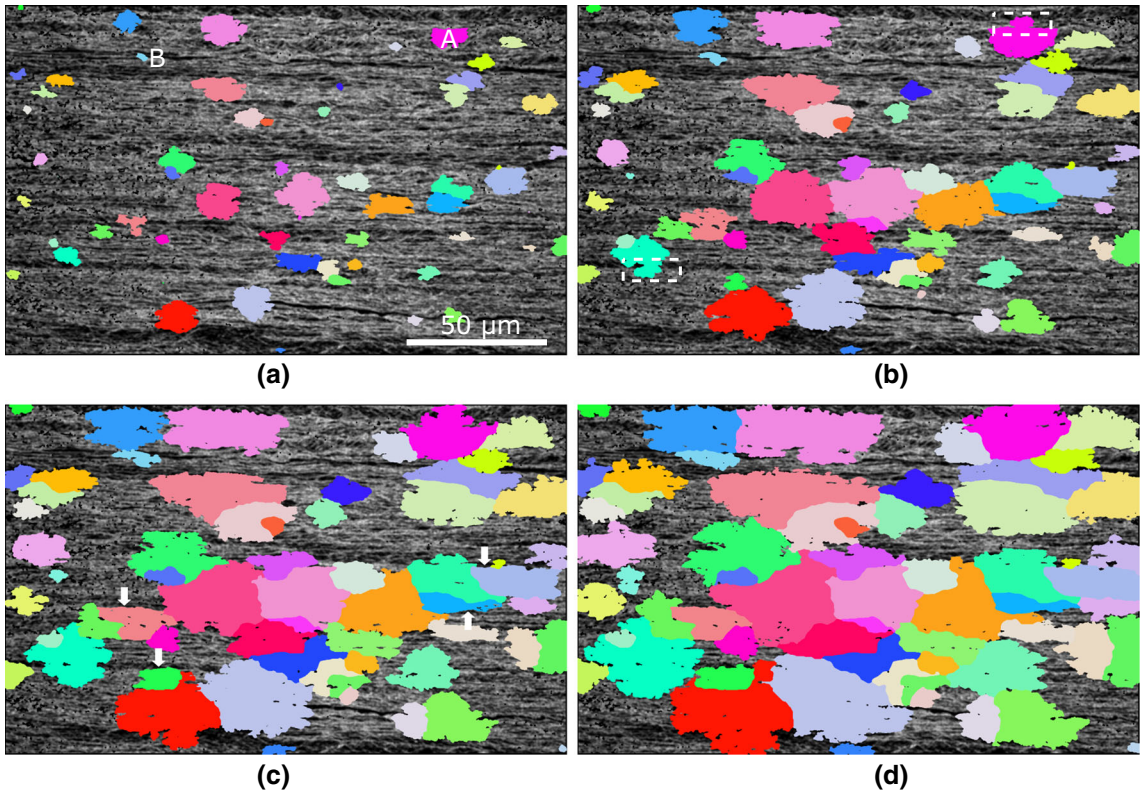

Fig. 7—Simulated microstructural evolution. The recrystallized fraction in (*a*) through (*d*) is 10, 30, 50 and 70 pct. The recrystallized grains are colored, while the gray shading of the deformed matrix shows the distribution of stored energy. The rectangles in (*b*) mark two regions with important protrusions. The arrows in (*c*) mark stationary boundaries.

$$f_i|_{t+\Delta t} = f_i|_t + \sum_{j=1}^{rx} \left(\frac{v_j \Delta t}{C_S} \right), \qquad [7]$$

where rx is number of recrystallized neighbors and v_j is the velocity of the GB segment separating each one of them from the central cell with label i (Figure 6). The status of the central cell changed from deformed to recrystallized as soon as $f_i \geq 1$. It was then counted among the recrystallized cells starting from the next time step.

To investigate how each feature of the model influenced the predictions of grain growth, several variants of the model were compared. The simulation was repeated either with or without considering the GB misorientation effect on its mobility. Also, the contribution of the capillarity force P_{GB} was either accounted for or disregarded. Finally, three alternative distributions of the stored energy were considered. For the first case, the CA model used the heterogeneous stored energy field directly from experimental measurement (see Figure 1(b)). For the second case, the stored energy field was uniform while keeping the average stored energy of the map unchanged: $\langle P_E \rangle_\Omega = 2.5 \text{MJ/m}^3$. For the third case, the total amount of stored energy was still the same as the experimental one, but the local heterogeneity was artificially amplified: the scaled stored energy field was calculated as $k \exp(P_E)$, where P_E was the experimentally determined stored energy, and $k = \langle P_E \rangle_\Omega / \langle \exp(P_E) \rangle_\Omega$.

The stored energy distributions are shown in Figure 4(b) in the form of histograms and cumulative distribution functions. The experimentally measured stored energy shows a distribution ranging from 0.5 to 6.2MJ/m^3. The scaled field distribution is much broader: the stored energy of about 40 pct of the map is less than 1.2MJ/m^3, whereas it is larger than 5.5MJ/m^3 for 10 pct of the map.

The high-resolution calculations were feasible using a parallel version of the CA model[71] and the introduction of an automatic time step adaptation algorithm.[72] The parameters of the CA model were identified based on an inverse analysis aiming to reproduce the experimentally observed recrystallization kinetics. Then, to provide comparable results of calculations under various investigated conditions, the numerical study assumed site-saturated nucleation: the number of nuclei was decided at the start of the simulation. The recrystallized nuclei were assigned crystal orientations as well as locations in the deformed microstructure, which were both randomly selected, but remained the same in all the case studies. Using the same set of nuclei in all simulations, minimized stochastics that could otherwise complicate the comparative interpretation of the predictions corresponding to different assumptions about grain growth, *i.e.* to different variants of the model.

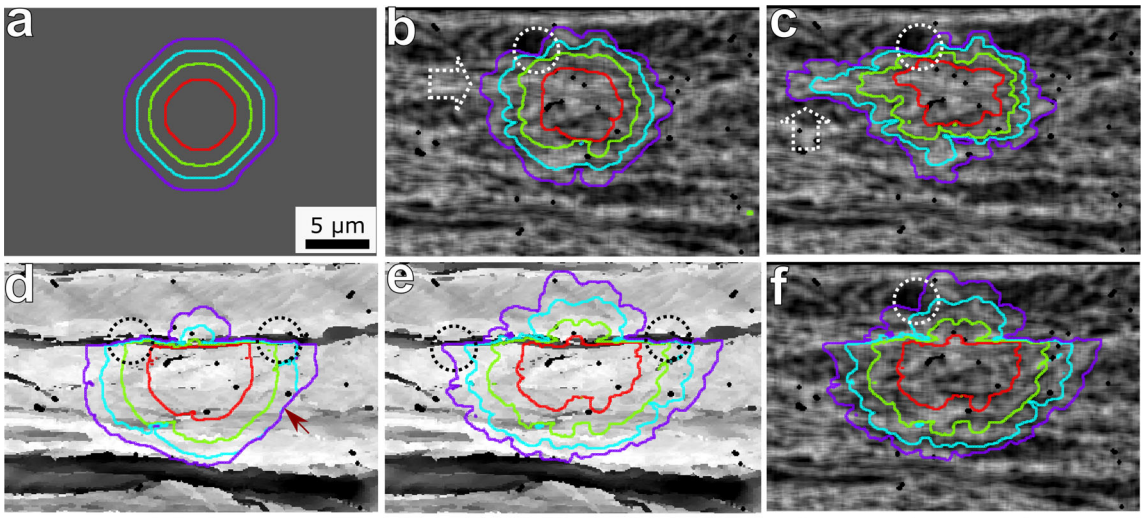

	a	b	c	d	e	f
P_E	uniform	hetero	scaled	uniform	hetero	hetero
M_G	uniform	uniform	uniform	hetero	hetero	hetero
P_{GB}	no	no	no	no	no	no

Fig. 8—Typical predictions of grain growth when disregarding the influence of GB curvature (capillarity force). Contour lines in red, green, cray, and purple represent the GB when the recrystallized fraction is 10, 20, 30, and 40 pct, respectively. Stored energy and GB mobility used in the model are listed in the table below the figure. GB mobility is assumed uniform in (*a*) through (*c*) and heterogeneous in (*d*) through (*f*). The background shading scales with the local stored energy in (a) through (c) and (f), and with the local misorientation relative to the recrystallized grain in (d) and (*e*). The non-linear scale bar of stored energy applies to (c) only. The circles in (*b*) through (f) mark places where growth was inhibited. The arrows in (b) and (c) mark places where protrusions formed inside a high stored energy band. The boundary segment marked by the arrow in d) became stationary when it came in contact with a neighboring recrystallized grain (not shown) (Color figure online).

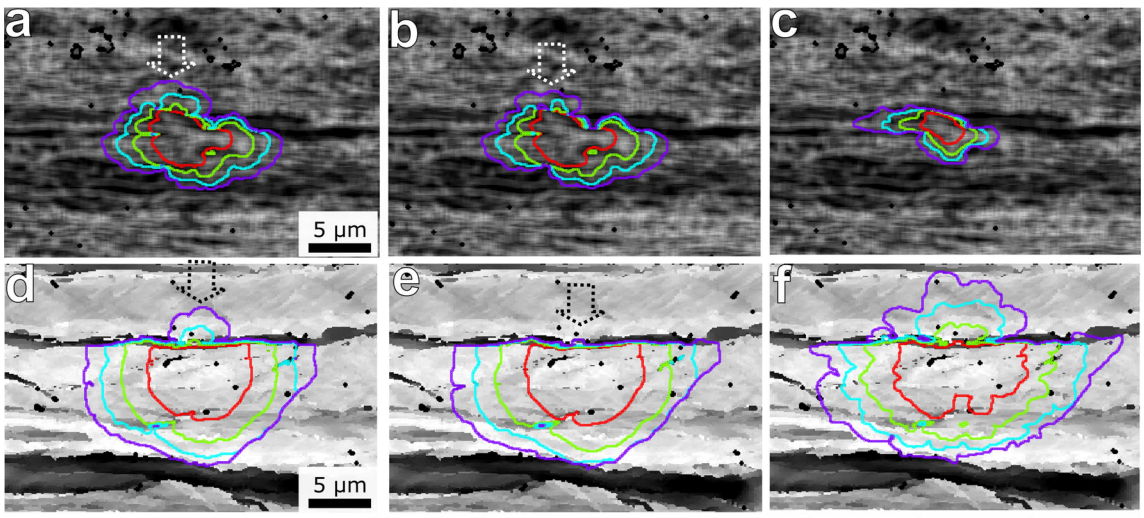

	a	b	c	d	e	f
P_E	hetero	hetero	hetero	uniform	uniform	hetero
M_G	uniform	uniform	hetero	hetero	hetero	hetero
P_{GB}	no	yes	yes	no	yes	yes

Fig. 9—Illustration of the influence of the capillarity force on the roughness of the boundaries of recrystallized grains. Two grains are considered: (*a*) through (*c*) present the grain marked "B" in Fig. 7a shown on the background of stored energy field and (*d*) through (*f*) correspond to the grain marked "A" shown on the background of local misorientation relative to the recrystallized grain. The influence of the boundary curvature on mobility is disregarded in (a) and (d). Stored energy and GB mobility used in the model are listed in the table below the figure. The arrows mark places where the capillarity force tends to prevent the formation of protrusions.

IV. SIMULATION RESULTS

Figure 7 shows an example of microstructure evolution predicted by the CA model when accounting for the experimental field of stored energy, the heterogeneity of GB mobility and GB curvature. The model predicted some protrusions that bridged across a deformation band unfavorable for growth. With these protrusions, a grain reached another band where its growth resumed. Two examples of such protrusions are marked by dotted rectangles in Figure 7b. By comparing different steps in the simulation, we can identify boundary segments that became stationary. Some are marked by arrows in Figure 7c. Due to such non-uniform boundary migration, many small islands of unrecrystallized material were embedded inside recrystallized grains, which was also seen experimentally.

A. *Boundary Migration of Individual Grains*

Figures 8 and 9 present a close up on the progressive growth of a recrystallized grain (marked "A" in Figure 7(a)), showing the typical microstructural evolution that is predicted under each investigated variant of the CA model. The influence of GB curvature on grain growth is disregarded in Figure 8 and is accounted for in Figure 9. Simulations presented in Figures 8(a) through (c) assumed uniform mobility of all GB segments, whereas mobility was considered to depend on misorientations across grain boundaries in Figures 8(d) through (f). The heterogeneity of stored energy gave rise to protrusions (as highlighted by an arrow in Figures 8(b) and (c)) but also retrusions (as marked by dotted circles in Figures 8(b) and (c)). This resulted in rough boundaries, especially when using the scaled stored energy field. Retrusions occurred nearby deformed regions with low stored energy that retarded invasion. On the other hand, the recrystallized grains remained rather equiaxed in Figures 8(a) through (c) as compared to Figures 8(d) through (f) where a much less isotropic grain growth resulted from the influence of the misorientation on the mobility of GB segments. The result shown in Figure 8(d) was obtained assuming homogeneous stored energy, and the shape of the recrystallized grain was thus dictated only by heterogeneous mobility. Growth was hindered on the top side of the recrystallized grain because nearby deformation bands had a low misorientation relative to this grain. There was initially a short GB segment with higher mobility that bridged across the low misorientation region and grew inside another band further on the top. Figures 8(e) and (f) show the growth predicted when both boundary mobility and stored energy were heterogeneous. When comparing all variants of the model, GB mobility was found to determine the overall grain shape, whereas stored energy was responsible for boundary roughness. As shown in Figure 9, the main effect of the capillarity force was to hinder the formation of protrusions, and this occurred both in the case of a uniform (Figures 9(a) and (b)) and a heterogeneous (Figures 9(d) and (e)) GB mobility. Such effect of GB curvature was obviously absent when both stored energy and boundary mobility were assumed uniform as the shape of recrystallized grains was then always circular, independent of the capillarity force. The final shape of the grain was determined by all three parameters: stored energy, boundary mobility, and the capillarity force of the grain boundary.

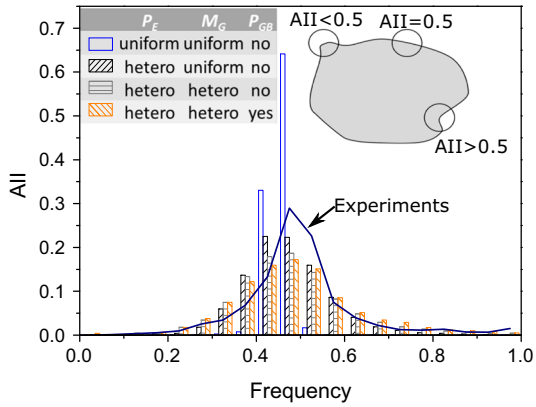

Fig. 10—Comparison of the boundary roughness stemming from simulations and experiments. The definition of AII is schematically shown in the insert, and the sampling radius used is 1.5 μm. The continuous line and the histograms show the statistical distribution of AII values after 35 min annealing at 423 K corresponding to a recrystallized fraction of 10 pct.

B. *Boundary Roughness*

The predicted GB roughness was compared to the experimental observations in the EBSD map using the area integral invariant (AII). AII was first used in digital image computing,[73] and recently introduced to characterize grain boundary roughness.[74] As schematically shown in the inset of Figure 10, AII was determined by drawing a circle with a specified radius (termed sampling radius) centered at a given position along the grain boundary. AII is the area fraction of the circle located inside the grain. The values of AII range between 0 and 1, and a value close to 0.5 indicates that the boundary segment is straight if a proper sampling radius was chosen. The AII value is less than 0.5 nearby a protrusion, whereas a retrusion causes AII $>$ 0.5. The sampling radius was set equal to 1.5μm to capture the desired features of the grain boundary. The continuous line in Figure 10 is the experimentally determined distribution of AII values for the grain shown in Figure 2(c). The curve peaks at about 0.5, representing the large fraction of straight boundaries seen in Figure 2(c). The broad distribution of AII values is not symmetric around the peak. The longer tail on the right indicates that sharp retrusions exist. The distributions of AII obtained from the CA simulation results when the recrystallized fraction is 10 pct are shown with histograms. When the stored energy was assumed uniform, the AII values had a very narrow distribution without protrusions and retrusions. Otherwise, both stored energy variation and GB mobility variation broadened the range of AII values. Introducing the influence of GB curvature only slightly affected the AII

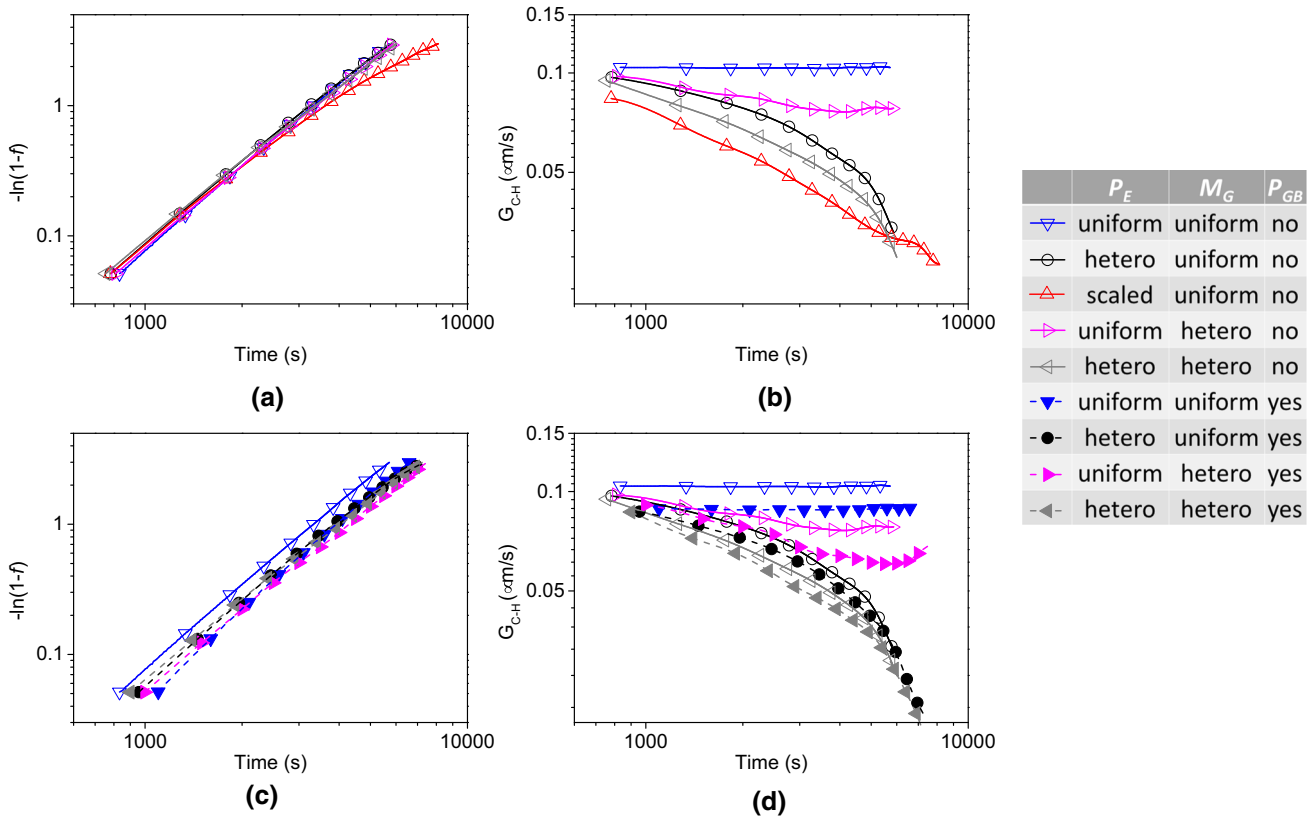

Fig. 11—Predicted recrystallization kinetics while using nine varians of the CA model. The stored energy field is either uniform, heterogeneous or scaled, the GB mobility is either uniform or heterogeneous, and the capillarity force is either accounted for or disregarded. (*a*) and (*c*) show Avrami plots of the recrystallized fractions. (*b*) and (*d*) show the evolution of the Cahn–Hagel growth rate (G_{C-H}), *i.e.*, the average boundary migration velocity of un-impinged recrystallizing boundaries.

distribution. Compared with experimental results, the simulations tended to slightly underestimate the proportion of straight boundary segments.

C. *Recrystallization Kinetics*

Figure 11 shows the predictions of the overall recrystallisation kinetics when relying on the model's different variants. The influence of the capillarity force P_{GB} is neglected in Figures 11(a) and (b) (as was done in Figure 8), and it is accounted for in Figures 11(c) and (d) (corresponding to the model variants shown in Figure 9). In Figures 11(a) and (c), the increase of the recrystallized volume fraction is presented as an Avrami plot, *i.e.* $-\ln(1-f)$ v.s. time t on a log-log scale. When P_{GB} is neglected, the differences between the investigated variants of the model are hardly visible in such a plot (Figure 11(a)). Most of them follow a rather straight line corresponding to an Avrami exponent $n \cong 2$, which is the theoretical value for growth in 2D with site-saturated nucleation. Using the scaled stored energy field, a deviation from the straight line occurs in the late recrystallization stages, and the Avrami exponent decreases from 2 to 1.5. Differences between the different variants of the model are much better seen when relying on the Cahn-Hagel growth rate. The Cahn-Hagel growth rate for the simulated results were calculated using Eq. [2], while S_V was obtained by line-intercept on the simulated images. As expected from theoretical models, the CA model predicts a constant G_{C-H} value when assuming a uniform stored energy field, otherwise G_{C-H} decreases over time. Accounting for heterogeneous grain boundary mobility contributed to further decreasing the Cahn-Hagel growth rate. The increasing proportion of immobilized grain boundary segments led to the progressive decrease of G_{C-H}. The effect of the capillarity force (shown in Figures 11(c) through (d)) was also to reduce the predicted growth rate, slowing down the recrystallization kinetics. Interestingly, when the effects of grain boundary curvature were considered, the value of the Avrami exponent showed stronger dependence on the stored energy field and on variations of boundary mobility.

V. DISCUSSION

A. *Influence on Grain Morphology*

As shown in Figures 8 and 9, the shapes of recrystallized grains predicted by the proposed CA model bear similarities with those observed experimentally. By accounting for the heterogeneous field of stored energy as well as GB mobility related to the misorientations, the CA model has produced more irregular grain shapes, closer to the experimental observations. The sensitivity

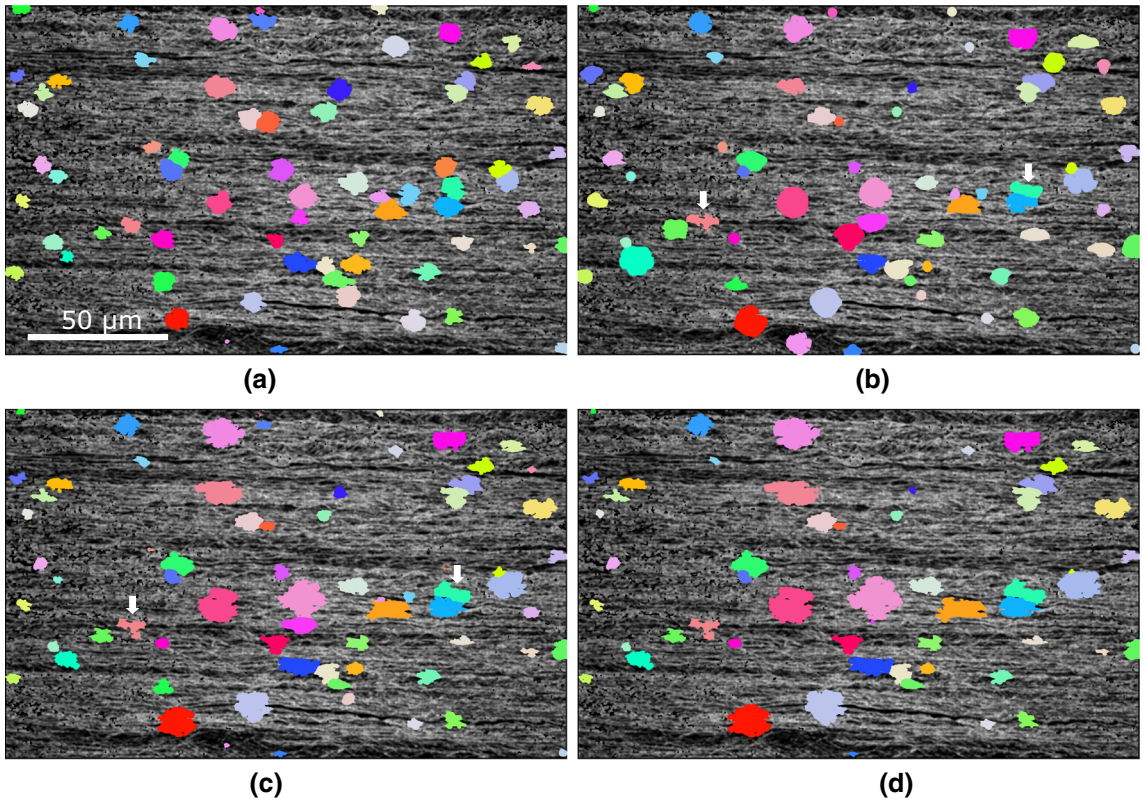

	a	b	c	d
P_E	hetero	uniform	hetero	hetero
M_G	uniform	hetero	hetero	hetero
P_{GB}	no	no	no	yes

Fig. 12—Simulated microstructure when the recrystallized fraction equals to 10 pct. The recrystallized grains are colored, while the gray shading of the deformed matrix shows the distribution of stored energy. The arrows in (*b*) and (*c*) mark some typical grains with grain shapes more affected by GB mobility (Color figure online).

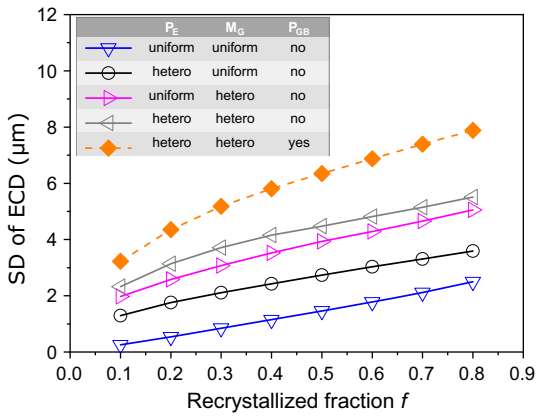

Fig. 13—Standard deviation (SD) of the equivalent circular diameter (ECD) of the 70 recrystallized grains as a function of the recrystallized fraction for simulations under various assumptions.

analysis showed that the best predictions were obtained when the effects of a heterogeneous driving force for recrystallization, which was associated with stored energy gradients and GB curvature, were combined to the effects of the heterogeneous mobility of GB segments, which was linked to the local misorientations.

Heterogeneity of GB mobility was found to influence most the average shape of recrystallized grains, whereas heterogeneity of stored energy was the main cause of GB roughness. This is seen when comparing Figures 8(d) and (e). More examples can be found in Figure 12, which compares simulations under different assumptions when the material is 10 pct recrystallized. The variations of grain sizes and shapes (*e.g.*, aspect ratio) are larger when the model accounts only for the heterogeneity of GB mobility (Figure 12(b)) than when it rather considers only the heterogeneity of stored energy (Figure 12(a)). The overall shapes of many grains seen in Figure 12(b) are retained in Figure 12(c), when both stored energy and GB mobility are considered heterogeneous. Two typical examples are marked by arrows in Figures 12(b) and (c). According to the comparison of Figures 12(c) and (d), the influence of boundary curvature on grain shapes is not significant. However, the size distribution is slightly broadened when GB migration depends on the local curvature. Indeed, considering local curvature tends to enlarge large grains, and shrink small grains. Some tiny grains

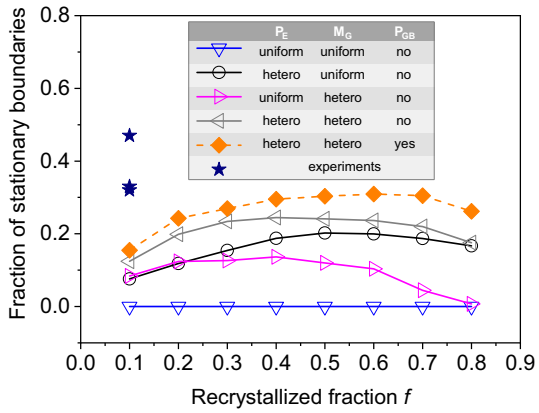

Fig. 14—Predicted fraction of stationary grain boundaries as a function of the recrystallized fraction, compared with the experimental observations.

seen in Figure 12(c) even disappear in Figure 12(d). Figure 13 shows the influence of different factors on grain size distributions using the standard deviations (SD) of the equivalent circular diameter (ECD) of recrystallized grains. GB mobility heterogeneity increases the SD of ECD by about 2 μm (the magenta curve), whereas stored energy heterogeneity only increases the SD of ECD by about 1 μm (the black curve). GB curvature only slightly increases the SD and ECD in the beginning of recrystallization, when comparing the gray and orange curves, but the influence of GB curvature increases as recrystallization continues, which might be explained by the fact that the extra negative driving force for bigger grains decreases as they grow, whereas smaller grains remain hindered by a large negative driving force, and they thus grow slowly. Therefore, the size distribution becomes broader as recrystallization continues when GB curvature is considered.

The present simulation work shows that GB mobility has a large influence on grain sizes and shapes, which was rarely reported in previous CA simulations. A possible reason is that GB mobility is assumed in most other CA simulations to be constant for high angle boundaries (HABs), and to vary only when misorientations are lower than 15 deg (*e.g.*, Reference [75]). Only in a few works, 40°⟨111⟩ boundaries were assumed to have a mobility a few times higher than the other HABs.[19,76] Under such assumptions, nuclei grow with almost constant GB mobility, because the majority of recrystallizing boundaries are neither low angle boundaries nor special HABs with uncommon mobility. In this work, we adopted a new relationship considering that mobility of HABs varies continuously with misorientation angles (Figure 4a), inspired by experimental measurements.[67] The variation in GB mobility then show significant influence on grain shapes and grain size distributions. In reality, GB mobility has even greater variations, depending not only on misorientation (angles and axes), but also on GB plane.[77] The latter is known as growth anisotropy. For recrystallization after low strains deformation, the misorientation between a recrystallized grain and the deformed matrix it grew into is more or less constant, but the different GB mobility of tilt/twist boundaries leads to non-equiaxed shape of recrystallized grains.[67,78] It may be expected that simulations accounting for greater heterogeneity of GB mobility would result in an even broader grain size distribution, as seen in the experimental results shown in this work and in previous work.[40,56] But more experimental or atomistic simulation data on dependence GB mobility are needed before this can be well adapted in CA models or other models for recrystallization.

Heterogeneity of stored energy is found to be the main cause of GB roughness. Previous experimental observations for recrystallization in matrix deformed to a low strain (cold-rolling to 20 pct thickness reduction) suggested that the scale of boundary roughness is related to the spacing of geometrically necessary dislocation boundaries.[79] This suggestion was confirmed by phase-field simulations.[41,80] For this work, the sample was deformed to a high strain, and the deformed matrix had a lamellar structure composed of dislocation boundaries, with an average lamellae thickness of 0.6 μm. The length scale of the boundary roughness for both simulated results and experimental results was related to the lamellae thickness.

B. *Influence on Grain Boundary Migration*

All of the three factors, stored energy variation, GB mobility and GB curvature, are found to contribute to the non-uniform migration of the recrystallizing boundaries. Figure 14 presents another quantitative comparison of the predictions to the experimentally observed non-uniform boundary migration. According to this figure, the fraction of boundary segments that are stationary already from an early stage of recrystallization is larger in the experimental map than in the model predictions. Only those GB segments not in contact with other recrystallized grains were considered. Experimentally, this fraction was deduced from the comparison of two EBSD maps of the same region scanned, respectively, after 5 and 10 pct overall recrystallization. Three grains were considered in this case. The first one is shown in Figure 2(c) (containing 47 pct immobile GB segments), and the other two grains were analyzed in Reference [40]. For the CA simulation, all the 70 recrystallized grains were accounted for. Under the assumption of a uniform driving force, all GB segments remained mobile until they impinged another recrystallized grain (the blue line). When stored energy and GB mobility heterogeneity were considered separately, the two factors each resulted in about 10 pct stationary boundaries at the beginning of recrystallization (black and magenta curves). The fraction of predicted stationary boundaries gradually increased to 20 pct as the recrystallized fraction increased to 50 pct under the assumption of stored energy variation alone, whereas the fraction of predicted stationary boundaries did not increase when considering only the heterogeneity of GB mobility. The latter fraction gradually decreased when recrystallized fraction was larger than 60 pct, since the stationary boundaries impinged other recrystallized grains, and were then not counted. The different trends

under the assumptions of heterogeneous stored energy and GB mobility indicate that stationary boundaries due to low local stored energy are likely to accumulate during recrystallization. Indeed regions with low stored energy may resist recrystallization, whereas regions with unfavorable misorientations to one of the recrystallized grain may have favorable misorientation to another recrystallized grain. When the heterogeneity of both stored energy and GB mobility was considered, the fraction of stationary GB segments was slightly raised. The same occurred when accounting for the effect of GB curvature on the driving force. All predicted values were, however, remain below experimental measurements.

The reason why the model underestimates the fraction of stationary GB segments might be discussed in two aspects. The first one is the simplified assumption according to which GB mobility depends on the amplitude of the misorientation and not on the axis of misorientation, nor on the tilting of this axis relative to the GB normal.[81] However, significant anisotropy of grain boundary mobility exists. For face centered cubic metals, the highest mobility were observed for boundaries with ⟨111⟩ misorientation axes, misorientation angles around 40°, and boundary planes normals perpendicular to the misorientation axes (*i.e.* approximately Σ7 tilt boundaries). The present work only considered the dependence of mobility on the misorientation angles, whereas it has been shown that mobility decreases sharply as the misorientation axis deviates from ⟨111⟩[67]. Molecular dynamics simulations showed that mobility depends strongly on both misorientation axes and boundary plane.[77] Some boundaries, including all the ⟨111⟩ twist boundaries, were immobile within the resolution of the simulation. More accurate account of the influence of the GB characteristics is likely to induce more heterogeneous velocities of the GB segments, consistent with experiments. However, 3D simulations are required to account for boundary plane normal (*i.e.* twist or tilt boundaries). The second reason for the mismatch between model and experiment is the fact that the simulation was performed in 2D whereas the reality is 3D. The reasons for the immobilization of some GB segments may be hidden in a 2D cross-section across the microstructure.[82] The GB curvature, in particular, can easily be underestimated inside a 2D cross-section. If a GB bulges outward, the unseen out-of-plane curvature may contribute to the pinning some GB segments due to the capillarity force.

C. *Influence on Recrystallization Kinetics*

The CA model predicted a decrease of the grain growth rate but not to the same extent as in experimental observations. As shown in Figure 11(a), according to the numerical simulations, the Avrami exponent decreased only slightly in the course of recrystallization. The steadily increasing proportion of immobile boundary segments obviously contributed to slowing down grain growth. Increasing this proportion, as discussed in the previous paragraph, would improve the match between the model and the experiments. Moreover, some recent experimental work[83,84] have contested the classical theory, which was established based on bicrystal experiments, rather suggesting that migration in polycrystals is influenced by interconnections in the GB network. Based on atomic scale simulations, Chen *et al.*[85] have recommended to characterize grain boundary mobility as a tensor instead of a scalar. All these new results are likely to improve predictions of the present recrystallization model.

VI. CONCLUSIONS

Different variants of a CA model were used in order to model SRX and investigate the sensitivity of GB migration to the heterogeneity of stored energy, GB mobility, and GB curvature. A high purity copper sample cold-rolled to 90 pct reduction in thickness and isothermally annealed at 423 K was used to assess the model predictions. EBSD mapping of the deformed microstructure served as input for the CA simulations. Comparison of experiments and modeling results showed that:

- The CA model produced grain shapes and GB roughness of recrystallized grains, which included protrusions and retrusions similar to those observed in the EBSD map. Heterogeneity of GB mobility was found to influence the most shapes of recrystallized grains and grain size distributions, whereas heterogeneity of stored energy was the main cause of GB roughness. The scale of GB roughness was related to the scale of stored energy variation. GB curvature tended to increase the range of grain size distributions.
- Growing recrystallized grains were progressively surrounded by an increasing proportion of immobilized GB segments when using variants of the CA model that accounted for both the non-uniform stored energy and the heterogeneous GB mobility. Compared with stationary boundaries due to low mobility, stationary boundaries due to low local stored energy had higher tendency to maintain till the end of recrystallization. However, the proportion of stationary boundaries remained lower than experimental findings.
- The CA model predicted a progressive decrease of the average GB migration velocities in the course of recrystallization. However, overall, deviations relative to the simple JMAK theory remained minor. The experimentally observed, significant decrease of the growth rate of recrystallized grains was not captured by the model. It is expected that improved predictions of the recrystallization kinetics would be obtained by simulating 3D microstructures and by enriching the dependence of mobility on the GB characteristics.

ACKNOWLEDGMENTS

FXL acknowledges the funding from the European Research Council (ERC Grant Agreement No.788567 M4D). LM acknowledges the financial assistance of the National Science Centre Project No. 2017/27/B/ST8/00373. LD is mandated by the FSR-FNRS (Belgium). Prof. Dorte Juul Jensen, Prof. Andy Godfrey and Dr. Yubin Zhang are highly acknowledged for fruitful discussions.

FUNDING

Open access funding provided by Karlstad University.

CONFLICT OF INTEREST

On behalf of all authors, the corresponding author states that there is no conflict of interest.

OPEN ACCESS

REFERENCES

1. Y. Wang, M. Chen, F. Zhou, and E. Ma: *Nature*, 2002, vol. 419(6910), pp. 912–15.
2. Y. Li, Y. Zhang, N. Tao, and K. Lu: *Scripta Mater.*, 2008, vol. 59(4), pp. 475–78.
3. J. Zhang, D. Raabe, and C.C. Tasan: *Acta Mater.*, 2017, vol. 141, pp. 374–87.
4. K. Huang, K. Zhang, K. Marthinsen, and R. Logé: *Acta Mater.*, 2017, vol. 141, pp. 360–73.
5. L. Xie, T. Huang, L. Zhang, W. Cao, G. Wu, and X. Huang: *Mater. Sci. Eng. A*, 2018, vol. 738, pp. 190–93.
6. S. Kheiri, H. Mirzadeh, and M. Naghizadeh: *Mater. Sci. Eng. A*, 2019, vol. 759, pp. 90–96.
7. F. Lin, Q. Shi, and L. Delannay: *Int. J. Solids Struct.*, 2020, vol. 184, pp. 167–77.
8. R. Doherty, D. Hughes, F. Humphreys, J.J. Jonas, D. Juul Jensen, M. Kassner, W. King, T. McNelley, H. McQueen, and A. Rollett: *Mater. Sci. Eng. A*, 1997, vol. 238(2), pp. 219–74.
9. E. Lauridsen, H. Poulsen, S. Nielsen, and D. Juul Jensen: *Acta Mater.*, 2003, vol. 51(15), pp. 4423–35.
10. J.J. Jonas, X. Quelennec, L. Jiang, and É. Martin: *Acta Mater.*, 2009, vol. 57(9): 2748–56.
11. Y. Lü, D.A. Molodov, and G. Gottstein: *Acta Mater.*, 2011, vol. 59(8), pp. 3229–43.
12. F. Lin, Y. Zhang, N. Tao, W. Pantleon, and D. Juul Jensen: *Acta Mater.*, 2014, vol. 72, pp. 252–61.
13. M. Miszczyk, H. Paul, J. Driver, and P. Drzymała: *Acta Mater.*, 2017, vol. 125, pp. 109–24.
14. B. Radhakrishnan, G. Sarma, and T. Zacharia: *Acta Mater.*, 1998, vol. 46(12), pp. 4415–33.
15. D. Raabe: *Annu. Rev. Mater. Sci.*, 2002, vol. 32(1), pp. 53–76.
16. M. Bernacki, Y. Chastel, T. Coupez, and R.E. Logé: *Scripta Mater.*, 2008, vol. 58(12), pp. 1129–32.
17. M. Bernacki, R.E. Logé, and T. Coupez: Scripta Mater., 2011, vol. 64(6), pp. 525–28.
18. K. Piękoś, J. Tarasiuk, K. Wierzbanowski, and B. Bacroix: *Comput. Mater. Sci.*, 2008, vol. 42(4), pp. 584–94.
19. M. Kühbach, G. Gottstein, and L. Barrales-Mora: *Acta Mater.*, 2016, vol. 107, pp. 366–76.
20. D.N. Ilin, N. Bozzolo, T. Toulorge, and M. Bernacki: *Comput. Mater. Sci.*, 2018, vol. 150, pp. 149–61.
21. H. Buken and E. Kozeschnik: *Metall. Mater. Trans. A*, 2017, vol. 48A(6), pp. 2812–18.
22. T. Takaki and Y. Tomita: *Int. J. Mech. Sci.*, 2010, vol. 52(2), pp. 320–28.
23. B. Zhu and M. Militzer: *Model. Simul. Mater. Sci. Eng.*, 2012, vol. 20(8), p. 085011.
24. W.A. Johnson: *Am. Inst. Min. Metal. Petro. Eng.*, 1939, vol. 135, pp. 416–58.
25. M. Avrami: *J. Chem. Phys.*, 1939, vol. 7(12), pp. 1103–12.
26. A.N. Kolmogorov: *Bull. Acad. Sci. USSR. Math. Ser.*, 1937, vol. 1(3), pp. 355–59.
27. F. J. Humphreys and M. Hatherly: *Recrystallization and Related Annealing Phenomena*, Elsevier, New York, 2012.
28. P. Baral, M. Laurent-Brocq, G. Guillonneau, J.-M. Bergheau, J.-L. Loubet, and G. Kermouche: *Mater. Des.*, 2018, vol. 152, pp. 22–29.
29. E.A. Jägle anbd E.J. Mittemeijer: *Metall. Mater. Trans. A*, 2012, vol. 43A(4), pp. 1117–31.
30. J.-W. Park, H.-J. Jeong, S.-W. Jin, M.-J. Kim, K. Lee, J.J. Kim, S.-T. Hong, and H.N. Han: *Mater. Charact.*, vol. 133, pp. 70–76.
31. R. Vandermeer and D. Juul Jensen: *Acta Mater.*, 2001, vol. 49(11), pp. 2083–94.
32. R. Vandermeer and B. Rath: *Metall. Trans. A*, 1989, vol. 20A(3), pp. 391–401.
33. H. Stüwe, A. Padilha, and F. Siciliano Jr.: *Mater. Sci. Eng. A*, 2002, vol. 333(1–2), pp. 361–67.
34. D. Srolovitz, G. Grest, M. Anderson, and A. Rollett: *Acta Metall.*, 1988, vol. 36(8), pp. 2115–28.
35. M. Oyarzábal, A. Martínez-de Guerenu, and I. Gutiérrez: *Mater. Sci. Eng. A*, 2008, vol. 485(1–2), pp. 200–209.
36. P. Saidi, S. Shahandeh, and J.J. Hoyt: *Metall. Mater. Trans. A*, 2015, vol. 46A(7), pp. 2975–85.
37. Y. Zhang, A. Godfrey, and D. Juul Jensen: *Scripta Mater.*, 2011, vol. 64(4), pp. 331–34.
38. C. Kerisit, R.E. Logé, S. Jacomet, V. Llorca, and N. Bozzolo: *J. Microsc.*, 2013, vol. 250(3), pp. 189–99.
39. Y. Zhang, J.D. Budai, J.Z. Tischler, W. Liu, R. Xu, E. Homer, A. Godfrey, and D. Juul Jensen: *Sci. Rep.*, 2017, vol. 7(1), pp. 1–8.
40. F. Lin, Y. Zhang, W. Pantleon, and D. Juul Jensen: *Metall. Mater. Trans. A*, 2018, vol. 49A(11), pp. 5246–58.
41. N. Moelans, A. Godfrey, Y. Zhang, and D. Juul Jensen: *Phys. Rev. B*, vol. 88, p. 054103.
42. H.W. Hesselbarth and I. Göbel: *Acta Metall. Mater.*, 1991, vol. 39(9), pp. 2135–43.
43. C. Davies: *Scripta Mater.*, 1997, vol. 36(1), pp. 35–40.
44. R. Goetz and V. Seetharaman: *Metall. Mater. Trans. A*, 1998, vol. 29A(9), pp. 2307–21.
45. D. Raabe: *Philos. Mag. A*, 1999, vol. 79(10), pp. 2339–58.
46. G. Kugler and R. Turk: *Comput. Mater. Sci.*, 2006, vol. 37(3), pp. 284–91.
47. S. Ghosh, P. Gabane, A. Bose, and N. Chakraborti: *Comput. Mater. Sci.*, vol. 45(1), pp. 96–103.
48. M.S. Salehi and S. Serajzadeh: *Comput. Mater. Sci.*, 2012, vol. 53(1), pp. 145–52.
49. M. Kazeminezhad: *Mater. Sci. Eng. A*, 2008, vol. 486(1–2), pp. 202–07.
50. F. Han, B. Tang, H. Kou, J. Li, and Y. Feng: *J. Mater. Sci.*, 2013, vol. 48(20), pp. 7142–52.
51. P. Mukhopadhyay, M. Loeck, and G. Gottstein: *Acta Mater.*, 2007, vol. 55(2), pp. 551–64.

52. D. Raabe and R.C. Becker: *Model. Simul. Mat. Sci. Eng.*, 2000, vol. 8(4), p. 445.
53. K. Janssens: *Math. Comput. Simul.*, 2010, vol. 80(7), pp. 1361–81.
54. L. Sieradzki and L. Madej: *Comput. Mater. Sci.*, 2013, vol. 67, pp. 156–73.
55. M. Kühbach, L. Barrales-Mora, and G. Gottstein: *Model. Simul. Mater. Sci. Eng.*, 2014, vol. 22(7), p. 075016.
56. F.X. Lin, Y.B. Zhang, W. Pantleon, and D. Juul Jensen: *Philos. Mag.*, 2015, vol. 95(22), pp. 2427–49.
57. W. Truszkowski and J. Kr'Ol, B. Major: *Metall. Trans. A*, 1980, vol. 11A(5), pp. 749–58.
58. F.X. Lin, W. Pantleon, T. Leffers, and D. Juul Jensen: *Mater. Sci. Forum*, 2012, vol. 702, pp. 398–401.
59. A. Godfrey, N. Hansen, and D. Juul Jensen: *Metall. Mater. Trans. A*, 2007, vol. 38A(13), pp. 2329–39.
60. W.T. Read and W. Shockley: *Phys. Rev.*, 1950, vol. 78(3), p. 275.
61. N. Hansen: *Mater. Sci. Technol.*, 1990, vol. 6(11), pp. 1039–47.
62. D.A. Hughes and N. Hansen: *Acta Mater.*, 2000, vol. 48(11), pp. 2985–3004.
63. S.-Q. Deng, A. Godfrey, and W. Liu: *Acta Metall. Sin.*, 2016, vol. 29(4), pp. 313–19.
64. Y. Zhang, A. Elbrønd, and F. Lin: *Mater. Charact.*, 2014, vol. 96, pp. 158–65.
65. D. Juul Jensen: *Acta Metall. Mater.*, 1995, vol. 43(11), pp. 4117–29.
66. O. Engler: *Acta Mater.*, 1998, vol. 46(5), pp. 1555–68.
67. Y. Huang and F. Humphreys: *Acta Mater.*, 1999, vol. 47(7), pp. 2259–68.
68. J. Freudenberger, A. Kauffmann, H. Klauß, T. Marr, K. Nenkov, V.S. Sarma, and L. Schultz: *Acta Mater.*, 2010, vol. 58(7), pp. 2324–29.
69. K. Kremeyer: *J. Comput. Phys.*, 1998, vol. 142(1), pp. 243–63.
70. C. Zheng, N. Xiao, D. Li, and Y. Li: *Comput. Mater. Sci.*, 2008, vol. 44(2), pp. 507–14.
71. M. Sitko and K. Banaś, L. Madej: *Materials*, 2021, vol. 14(15), p. 4082.
72. M. Sitko and L. Madej: *J. Comput. Sci.*, 2021, vol. 54, p. 101437.
73. S. Manay, D. Cremers, Byung-Woo. Hong, A.J. Yezzi, and S. Soatto: *IEEE Trans. Pattern Anal. Mach. Intell.*, 2006, vol. 28(10), pp. 1602–18.
74. J. Sun, Y. Zhang, A. Dahl, K. Conradsen, and D. Juul Jensen: *J. Microsc.*, 2017, vol. 265(3), pp. 313–21.
75. C. Haase, M. Kühbach, L.A. Barrales-Mora, S.L. Wong, F. Roters, D.A. Molodov, and G. Gottstein: *Acta Mater.*, 2015, vol. 100, pp. 155–68.
76. E.A. Jägle and E.J. Mittemeijer: *Metall. Mater. Trans. A*, 2012, vol. 43A(7), pp. 2534–51.
77. D.L. Olmsted, E.A. Holm, and S.M. Foiles: *Acta Mater.*, 2009, vol. 57(13), pp. 3704–13.
78. G. Fan, Y. Zhang, J.H. Driver, and D. Juul Jensen: *Scripta Mater.*, 2014, vol. 72, pp. 9–12.
79. J. Sun, Y. Zhang, and D. Juul Jensen: *Scripta Mater.*, 2017, vol. 126, pp. 45–49.
80. V. Yadav, N. Moelans, Y. Zhang, and D. Juul Jensen: *Scripta Mater.*, 2021, vol. 191, pp. 116–19.
81. D.M. Saylor, B.S. El Dasher, A.D. Rollett, and G.S. Rohrer: Acta Mater., 2004, vol. 52(12), pp. 3649–55.
82. D. Juul Jensen and Y. Zhang: *Curr. Opin. Solid State Mater. Sci.*, 2020, vol. 24(2), pp. 100821.
83. J. Zhang, W. Ludwig, Y. Zhang, H.H.B. Sørensen, D.J. Rowenhorst, A. Yamanaka, P.W. Voorhees, and H.F. Poulsen: *Acta Mater.*, 2020, vol. 191, pp. 211–20.
84. A. Bhattacharya, Y.-F. Shen, C.M. Hefferan, S.F. Li, J. Lind, R.M. Suter, C.E. Krill III., and G.S. Rohrer: *Science*, 2021, vol. 374(6564), pp. 189–93.
85. K. Chen, J. Han, X. Pan, and D.J. Srolovitz: *Proc. Natl. Acad. Sci.*, 2020, vol. 117(9), pp. 4533–38.